Role of optical channeling in contrast enhancement of echo interferometers

Gehrig Carlse [*], Jaskaran Randhawa, Eduardo Ramos, Thomas Vacheresse, Alex Pouliot,
Adam C. Carew, and A. Kumarakrishnan [†]

Department of Physics and Astronomy, York University, Toronto, Ontario, Canada M3J 1P3

We investigate channeling oscillations in the contrast of a density grating formed by exposing a sample of ultracold atoms to an optical standing-wave pulse. We show that these dynamics can be imprinted on the echo signal associated with a two-pulse atom interferometer. Experimental results are supported by a simple model, which describes the grating contrast as the combination of two separate physical effects, namely, matter-wave interference and classical optical channeling resulting in Pendellösung-like oscillations. We discuss the enhancement in signal strength of echo interferometers that can be achieved by relying on these oscillations.

I. INTRODUCTION

Raman atom interferometers (AIs) have evolved into valuable tools for investigating inertial effects with unprecedented precision [1–5] and for tests of fundamental physics [6–8]. They have also become the primary technique used in state-of-the-art portable inertial sensors [9–15]. A potentially simpler experimental configuration that has achieved measurements of $\hbar/m$ and gravitational acceleration (g) with a sensitivity $\sim$1 order of magnitude lower than Raman AIs is the single-state echo-type AI [16–20]. Raman interferometers and related techniques that rely on large momentum transfer to the atomic sample can scatter several thousand photons per atom when the matter-wave fringes are detected. In comparison, the signal strength for echo AIs, which depends upon coherent scattering from a density grating, is limited to $\sim$1 photon per atom. Previous work relying on echo AIs has been further limited by the low contrast of these density gratings. Therefore, in order to bridge this gap in sensitivity with respect to other AIs, it is necessary to understand the basis for the grating contrast and explore how it can be enhanced.

In grating echo AIs, two standing-wave (SW) pulses, separated by a time T, illuminate an ultracold sample, resulting in diffraction of the momentum states separated by $2\hbar k$, where $k = 2\pi/\lambda$ is the wave vector and λ is the wavelength of light. The AI is characterized by the evolution of a density grating after each excitation pulse and the rephasing of the grating in the vicinity of the echo time $t = 2T$ in a manner reminiscent of a photon echo experiment [21], which is a general technique for canceling the velocity distribution of the sample. Unlike the photon echo experiment, which involves the excited state, the grating echo AI relies on a ground-state density grating arising from matter-wave interference that can be probed by a coherently backscattered readout pulse.

Figure 1 shows a schematic representation of the backscattered signal when the readout pulse is applied following either one or two excitation pulses. Ideally, when the excitation pulses are short enough to satisfy the Raman-Nath criterion, the momentum-state interference that produces the signal can be modeled using Kaptiza-Dirac diffraction of plane waves, an effect that was first demonstrated for atoms in Ref. [22].

Previous calculations have modeled the echo contrast in the Raman-Nath regime [16,17,20,23], on the basis of diffraction of atomic plane waves and by averaging over the velocity distribution of the sample to determine the density modulation of the wave function. While this approach is successful at modeling the signal shapes in the Raman-Nath limit, it provides an incomplete picture when the excitation pulses are longer. In this intermediate regime and in the well-studied long-pulse (Bragg) regime [24–27], there are two mechanisms at play, namely, the single-atom momentum-state interference and the response of the ensemble that produces channeling at the nodes of the SW potential [28]. These channeling oscillations have been previously observed in demonstrations of Bragg scattering with cold atoms [27,29] as well as in BEC experiments [30]. Work in the intermediate regime has shown a smooth transition between the Raman-Nath and Bragg regimes [27]. However, the increase in contrast associated with channeling has not been adequately quantified in grating echo experiments.

Among other related work with echo AIs, Ref. [31] explored the signal shapes by varying pulse parameters, while Ref. [32] investigated the increase in grating contrast that can be achieved by loading the cold sample into a lattice with a long pulse.

In this paper, we investigate a complementary technique that relies on intermediate-length SW pulses to produce Pendellösung-like channeling oscillations in the grating contrast. We study the basic features of these oscillations by probing the contrast of a density grating, due to a single pulse, whose dynamics can then be imprinted onto an echo signal in a two-pulse interferometer. Further, we show the unambiguous quadratic dependence of the signal on the

---

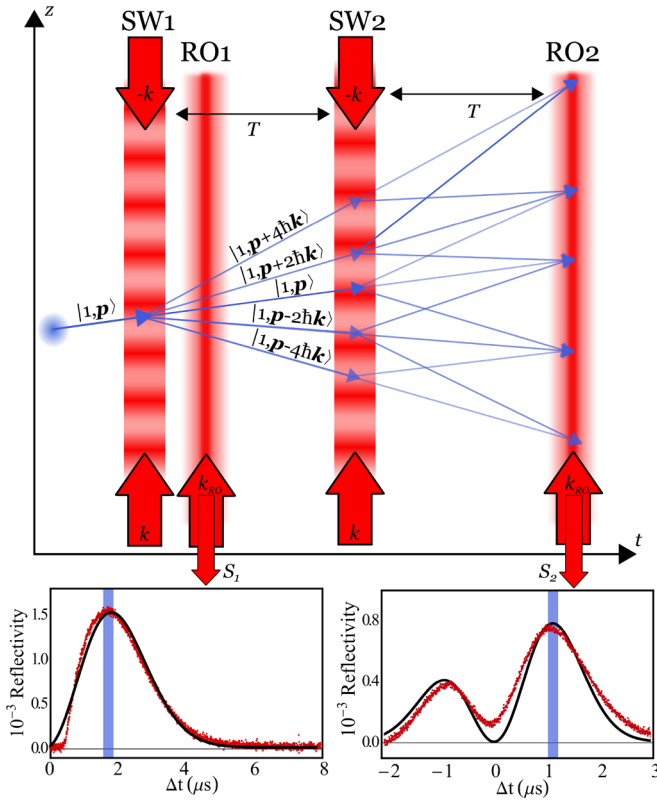[*]gehrig.carlse@gmail.com
[†]akumar@yorku.ca

FIG. 1. Schematic of standing-wave-induced atomic gratings in a cold sample. Momentum state diffraction of a generic ground state $|1, p\rangle$ is shown following the application of two standing-wave (SW, $\pm k$) pulses, along with the backscattering of a traveling-wave readout (RO, k_{RO}) pulse applied after either one or two SW pulses. The lower panels show experimental signals (red points) and theoretical calculations (solid black lines) for a sample of ^{85}Rb atoms with a temperature of $\sim 10 \, \mu$K in both one- and two-pulse configurations. Each panel also shows a vertical bar denoting the small integration window used to measure the peak reflectivity.

excitation pulse area within the Raman-Nath regime and identify improvements in contrast attributable to channeling when this regime is violated using longer excitation pulses. We explore how channeling using intermediate-length pulses can increase the reflectivity of the atomic sample in echo experiments. Our experimental results are supported by a simple model, which shows that the contrast can be described as the combination of two separate physical effects: matter-wave interference and classical optical channeling that produces Pendellösung-like oscillations.

In what follows, we present an overview of the experiment and an introduction of a simple theoretical model, followed by results and discussion.

II. EXPERIMENTAL SETUP

The experimental setup resembles the apparatus described in Ref. [33] and is shown in Fig. 2(a). A pyrex cell (~ 1 m in length) with rectangular faces contains room-temperature rubidium vapor. The system is pumped with an ion pump and locally heated such that the background pressure is $\sim 4 \times 10^{-9}$ Torr and the trap loading time is ~ 5 s. The trapping,
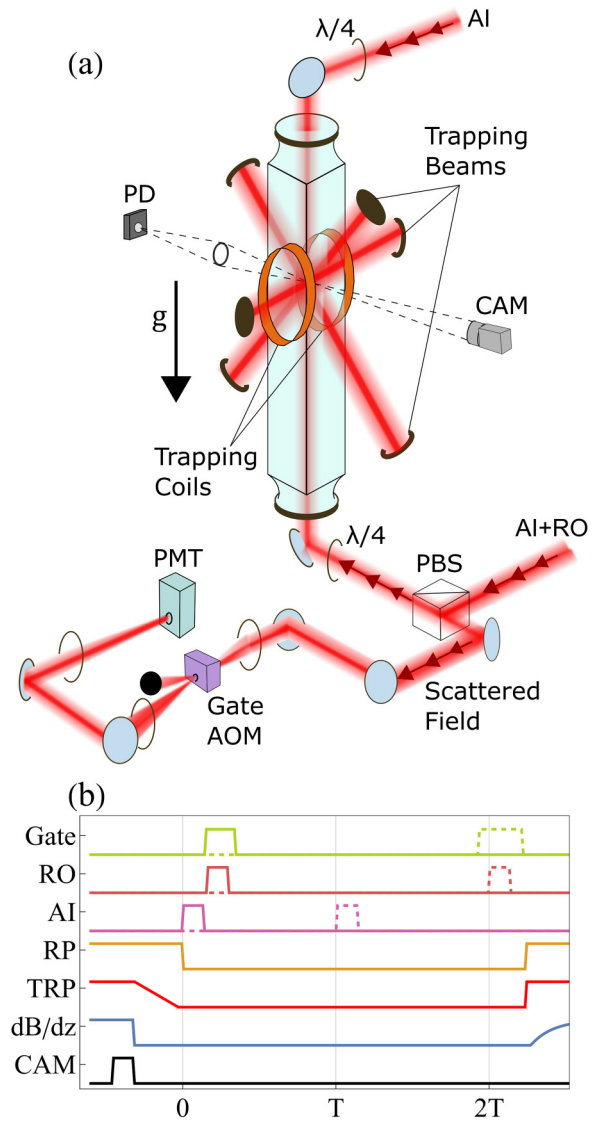

FIG. 2. (a) Sketch of pyrex trapping cell and AI layout that uses an AOM-gated-PMT for signal collection. The direction of g (along z) is shown with an arrow. Open circles: lenses; closed circles: mirrors; CAM: CCD camera; PD: photodiode; PBS: polarizing beam splitter; $\lambda/4$: quarter wave plate. (b) Timing sequence used for AI experiments. Dashed lines indicate additional pulses used for echo experiments. Gate: Electronic gate of PMT and gating AOM; RO: traveling-wave readout pulses; AI: SW excitation pulses; RP: repump laser, TRP: trapping laser; dB/dz: magnetic field gradient.

repump, and AI beams are generated using tapered amplifiers seeded with external cavity diode lasers [34,35] and shuttered by acousto-optic modulators (AOMs). After turning off the confining magnetic field gradient, the atoms are held in a molasses for 5.5 ms, while the trapping beams are further detuned by ~ 40 MHz to reduce heating. The vapor cell loaded magneto-optical trap (MOT) contains $\sim 10^9$ ^{85}Rb atoms at a temperature of $\sim 13 \, \mu$K, as determined by CCD imaging of the free expansion of the cloud [36].

The timing diagram for the AI experiment is shown in Fig. 2(b). The circularly polarized SW excitation pulses (blue detuned between 100 and 400 MHz with respect to the $F =$

$3 \rightarrow F' = 4'$ transition in ^{85}Rb) and the traveling-wave read-out pulse (blue detuned ~ 50 MHz from the $F = 3 \rightarrow F' = 4'$ transition in ^{85}Rb) are generated from separate chains of AOMs and applied along the vertical direction, as shown in Fig. 2(a). Typically pulses use ~ 20 mW of optical power and have a beam waist of ~ 3 mm. The backscattered signal is diffracted into an electronically gated photomultiplier tube (PMT) using a 250 MHz AOM with an efficiency of $\sim 20\%$ and a rise time of ~ 100 ns. The electronic gate, which has a rise time of 200 ns, is engaged at the same time as the gating AOM with the readout pulse applied only after both the gate and the AOM are fully opened.

III. THEORETICAL MODEL

In this section, we describe two aspects of the backscattered signals, namely, the effect of matter-wave interference and the consequences of channeling in the SW potential. We combine these effects using a simple model to describe the density evolution of the sample and show how the contrast of the gratings can be maximized.

In the limit of short excitation pulses, the atoms sample only a highly localized portion of the spatially varying potential. In this case, the contribution from matter-wave interference has been analytically described in Refs. [16,20,23,31]. In all of these experiments, the backscattered electric field resulting from the matter-wave interference is proportional to the $k = 2$ Fourier component of the density distribution of the sample. When the readout is applied following a single SW pulse, the backscattered electric field, shown in Fig. 1, is given by

$$S_1 = re^{-(\Delta t/\tau_{\text{coh}})^2} E_{\text{RO}}^2 u_1^2 \sin^2(\phi - \theta)$$
$$\times [J_0(2u_1\omega_1) + J_2(2u_1\omega_1)]^2, \qquad (1)$$

where $\phi = \omega_q \Delta t$ is the recoil phase, $\omega_q = (2k)^2 \hbar / 2m$ is the recoil frequency, and m is the mass of the atomic species. The thermal coherence time of a sample with temperature $\mathcal{T}$ is given by $\tau_{\text{coh}} = (k\tilde{u})^{-1}$, where we define the most probable speed for an atom as $\tilde{u} = \sqrt{k_B \mathcal{T}/m}$. J_M is the Mth-order Bessel function of the first kind, E_{RO} is the electric field of the readout beam, θ is the phase shift of the scattered field signal arising from spontaneous emission during the excitation, $\omega_1 = \sqrt{\sin(\phi + \theta)\sin(\phi - \theta)}$, and r is a constant of proportionality. The signal envelope described by Eq. (1) is shown in the lower left panel of Fig. 1. The rise of the signal is associated with the evolution of the grating contrast and the fall represents the dephasing resulting from the velocity distribution. The overall width of the signal is parameterized by τ_{coh}. Note that in the case of a one-pulse grating, the relative time, $\Delta t = t - t_{\text{signal}}$, is simply t since the density grating begins to form at $t_{\text{signal}} = 0$. We also define $u_N = \Omega_0^2 \tau_N / 2\Delta$ as the two-photon area of the Nth excitation with a pulse width τ_N, Rabi frequency Ω_0, and single-photon detuning Δ. The quantity $\Omega_0^2 / 2\Delta$ is referred to as the atom-field coupling strength.

When the readout pulse is applied in the vicinity of the echo time, following two excitation pulses separated by a time
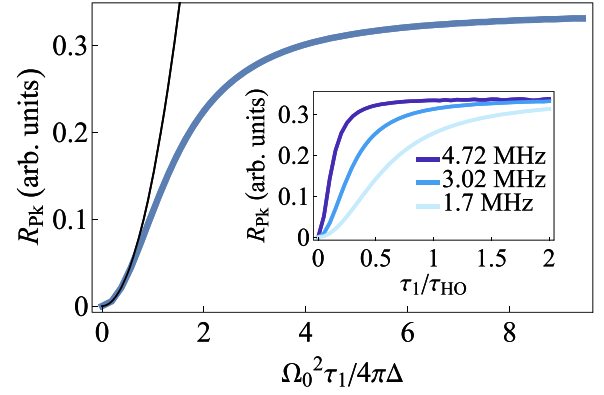

FIG. 3. Peak reflectivity of the atomic gratings in the Raman-Nath limit, described by Eqs. (1) and (2) as a function of the first pulse area, $u_1 = \Omega_0^2 \tau_1 / 2\Delta$. The black line is a second-order Taylor expansion of the reflectivity about $u_1 = 0$ showing the quadratic dependence of this quantity for small pulse areas. Inset: The same quantity as a function of excitation pulse duration, plotted as a fraction of τ_{HO} [see Eq. (3)]. Calculations are shown for a range of atom-field coupling strengths (see legend).

T, the backscattered field, also shown in Fig. 1, is given by

$$S_2 = re^{-(\Delta t/\tau_{\text{coh}})^2} E_{\text{RO}}^2 u_1^2 u_2^4 \sin^2(\phi + \theta) \sin^4(\phi + \omega_q T - \theta)$$
$$\times [J_0(2u_1\omega_1) + J_2(2u_1\omega_1)]^2$$
$$\times [J_0(2u_2\omega_2) + \tfrac{4}{3}J_2(2u_2\omega_2) + \tfrac{1}{3}J_4(2u_2\omega_2)]^2, \qquad (2)$$

where $\omega_2 = \sqrt{\sin(\phi + \omega_q T + \theta)\sin(\phi + \omega_q T - \theta)}$. The signal envelope described by Eq. (2) is shown in the lower right panel of Fig. 1. The minimum in the signal at $\Delta t = 0$ represents the replication of the phase grating created by the first standing-wave pulse. The double-peaked structure exhibits asymmetry in the relative height of the two lobes as a function of the pulse separation T, as well as the areas of the excitation pulses [17,23,31]. In the case of an echo experiment, the relative time refers to $\Delta t = t - 2T$ since the grating echo will form in the vicinity of $t_{\text{signal}} = 2T$.

The peak reflectivity R_{Pk}, which is a measure of the contrast of these gratings, can be obtained by integrating the total backscattered signal over a small time interval, as shown in Fig. 1. The peak reflectivity as a function of the first pulse area u_1, calculated on the basis of Eqs. (1) and (2) (for one- and two-pulse configurations, respectively), is shown in Fig. 3. The excitation pulse areas can be modified by changing either the pulse intensity (atom-field coupling strength) or pulse duration. The inset to Fig. 3 shows the peak reflectivity plotted as a function of pulse duration for a variety of atom-field coupling strengths. The pulse duration is shown as a fraction of the harmonic oscillator (HO) period [28,37],

$$\tau_{\text{HO}} = \pi / \sqrt{\Omega_0^2 \omega_q / \Delta}. \qquad (3)$$

When the Raman-Nath limit is well satisfied, the backscattered signal exhibits a quadratic dependence on the pulse area, as shown in Fig. 3. However, if the pulse durations violate the Raman-Nath limit, the atoms sample the spatial variation of the SW potential. In this case, the peak reflectivity is
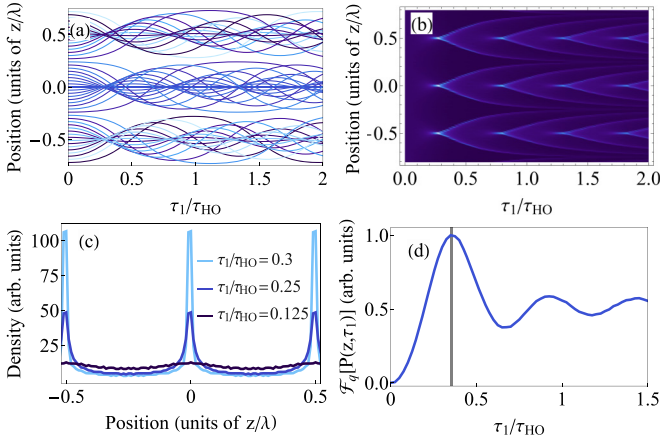
FIG. 4. (a) Center-of-mass trajectories of atoms in the far-off resonance channeling potential [Eq. (4)] as a function of excitation length. (b) Time evolution of atomic density distribution during Pendellösung-like channeling. (c) Histogram of population distribution across two lattice periods for several channeling times. (d) Backscattered signal estimated as the $q = 2$ (or $\lambda/2$) Fourier harmonic of the density distributions from (b) as a function of channeling time. The vertical bar shows the maximum predicted signal which occurs at $\tau_1 \sim 0.3\,\tau_{\mathrm{HO}}$.

dominated by channeling into the nodes of the potential. Under these conditions, the reflectivity would be expected to increase at the same rate with respect to τ_{HO}, irrespective of atom-field coupling. The differing rates of reflectivity saturation shown in the inset of Fig. 3 highlight the absence of channeling in Eqs. (1) and (2).

The effect of channeling can be explained on the basis of the following simple model. We consider the classical, center-of-mass motion of the atoms interacting with the SW along the z direction to be described by

$$m\ddot{z} = -\frac{\hbar k \Omega_0^2}{\Delta} \sin(2kz). \tag{4}$$

Figure 4(a) shows the trajectories of atoms channeled in this potential, from an initially uniform spatial distribution. These atomic trajectories lead to density modulation $P(z, \tau)$, in the sample which evolves as shown in Fig. 4(b). The grating contrast can be visualized by taking temporal slices of the sample density, as shown in Fig. 4(c). In a purely harmonic potential, the atoms would congregate at the nodes after $\tau = \tau_{\mathrm{HO}}/4$. Here, we observe the maximum contrast at $\tau \sim \tau_{\mathrm{HO}}/3$ since the atoms sample an anharmonic (sinusoidal) SW potential. The backscattered signal from such a density modulation can be modeled by the $q = 2$ Fourier component of the population distribution. Figure 4(d) shows the evolution of this reflected signal amplitude as a function of the channeling time. This plot is obtained by displaying the $q = 2$ Fourier component of each temporal slice of Fig. 4(b) for each value of the channeling time.

Here we note that this peak reflectivity, which stems from channeling, exhibits a modulation reminiscent of so-called Pendellösung oscillations [38], first linked to x-ray diffraction [39] and later observed in cold-atom experiments [29]. This signal will remain unchanged as a function of the
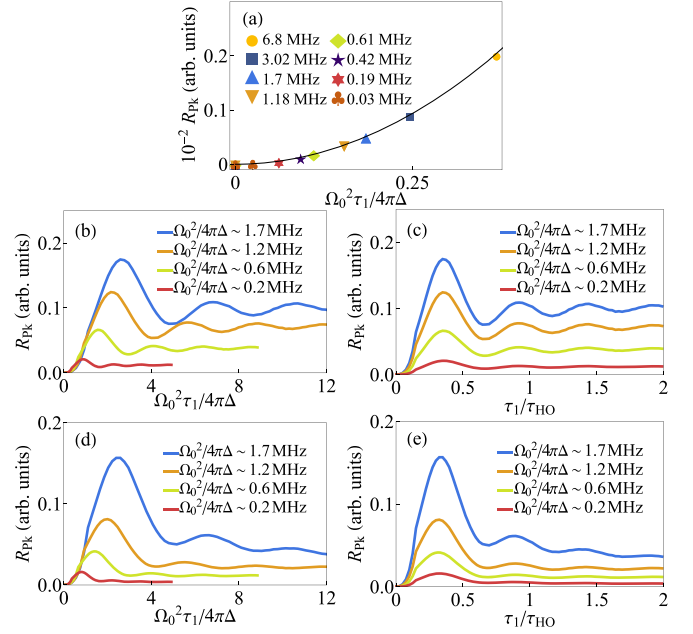

FIG. 5. Peak reflectivity calculated using Eq. (5) for a variety of atom-field coupling strengths shown in the legend. (a) Results for very small excitation pulse areas demonstrating the quadratic dependence (black line). (b) Results for a wider range of pulse areas. (c) Results plotted as a function of the excitation pulse length (shown as a fraction of τ_{HO}). Simulations use $\alpha = 1$ and $\tau_{\mathrm{RN}} = 0.15\,\tau_{\mathrm{HO}}$. (d) and (e) show the same calculations as (b) and (c), including an exponential decay of the form $Ae^{-C\tau_1} + B$ to incorporate the effects of experimental decoherence, with $A = 1$, $B = 0.3$, and $C = \Omega_0^2/2\Delta$.

atom-field coupling strength, as the atoms will be characteristically channeled on the timescale of Eq. (3). This is quite distinct from the prediction shown in the inset to Fig. 3, which represents the result of matter-wave interference, a signal that reaches a maximum value at different channeling times (with respect to τ_{HO}) for different atom-field coupling strengths.

We model the full sample density as the convolution of the independent position-space distributions arising from matter-wave interference and channeling. Using the convolution theorem, the scattered field signal from the AI can be written as the product of the q-space representation of each distribution,

$$S_{\mathrm{tot}}(\tau) = \alpha S_{\mathrm{chan}} \times S_N(\min[\tau, \tau_{\mathrm{RN}}]), \tag{5}$$

where α is a multiplicative factor that can be used to rescale the predicted reflectivity and compare to data, $S_{\mathrm{chan}} = \mathcal{F}_q[P(z, \tau)]$ is the $q = 2$ Fourier component of the density modulation resulting from channeling [see Fig. 4(d)], and S_N represents the scattered field signals described by either Eq. (1) ($N = 1$) or Eq. (2) ($N = 2$), respectively. Since the theoretical formalism underpinning Eqs. (1) and (2) relies upon the diffraction of plane waves in the Raman-Nath limit, we truncate the contribution of these matter-wave interference terms if the pulse durations become suitably long, where τ_{RN} represents the limit of the Raman-Nath regime.

Figure 5(a) shows the predictions for Eq. (5) for a range of atom-field couplings, for which the pulse durations are within the Raman-Nath limit. We note that the scattered field

is predicted to scale quadratically in this regime as a function of pulse area. This scaling suggests a useful method for identifying violations of the Raman-Nath criterion. We define the limit as $\tau_{RN} = 0.2\, \tau_{HO}$ in accordance with the extent of this quadratic trend.

Figure 5(b) shows the predictions of Eq. (5) as a function of pulse area for a variety of atom-field coupling strengths. Here the pulse durations are not limited to the Raman-Nath regime and extend well beyond this limit. It is evident that the oscillations seen in the signal amplitudes are out of phase for different atom-field coupling strengths if the pulse duration extends beyond the Raman-Nath limit. In comparison, Fig. 5(c) shows the same predictions plotted as a function of the excitation pulse width, in units of τ_{HO} for each atom-field coupling strength. Here, we note that the reflectivity reaches a maximum at a consistent fraction of the harmonic oscillator period and remains in phase for all pulse durations and coupling strengths, in contrast to predictions that do not consider channeling (see inset of Fig. 3).

To include contributions of experimental decoherence, such as possible excitation due to stray near-resonant photons and spontaneous emission during the excitation pulse, we augment the model by convolving Eq. (5) with a phenomenological exponential decay of the form $Ae^{-C\tau_N} + B$, where A and B are free parameters and C depends upon the coupling strength [40].

Figures 5(d) and 5(e) show the results of this refined model, with the reflectivity plotted as a function of the pulse area and pulse duration as a fraction of τ_{HO}, respectively. These panels show that the reflectivity approaches a steady-state value for long interaction times. It is apparent that the steady-state value is correlated with the atom-field coupling strength with the ratio of the steady-state value and that of the first maximum in the reflectivity being inversely related to the coupling strength. Figure 5(e) also highlights an additional effect of this decoherence, namely, a slight dephasing of the revivals in signal strength for different atom-field coupling strengths.

We test these predictions in the following section and identify the conditions under which the grating contrast can be maximized.

IV. RESULTS AND DISCUSSION

Figure 6(a) shows the peak reflectivity for the one-pulse experiment as a function of the pulse area in the Raman-Nath limit. As predicted by theory (see Fig. 3), there is a distinct quadratic dependence for a small pulse area, independent of atom-field coupling strength. Here we only display data for pulse durations of less than $0.2\, \tau_{HO}$, where the atomic motion is deemed to satisfy the Raman-Nath criterion.

Figure 6(b) shows the peak reflectivity for the one-pulse experiments over a wider range of pulse areas that violate the Raman-Nath criterion. In accordance with the simple model presented in Sec. III, the maximum reflectivity for a particular atom-field coupling is obtained with a distinct pulse area, in contrast to predictions that do not consider channeling (see Fig. 3). Comparing the largest attainable signals [shown in Fig. 6(b)] with the maximum reflectivity observed within the Raman-Nath limit [shown in Fig. 6(a)], we note that the reflectivity appears to be enhanced by ~2.5 times when the
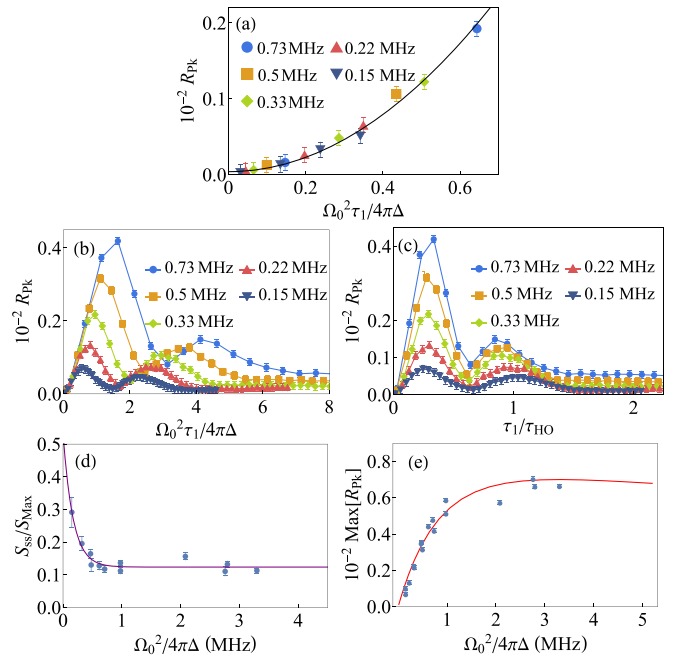

FIG. 6. Peak reflectivity measured in one-pulse grating experiments using a variety of atom-field coupling strengths ($\Omega_0^2/2\Delta$) shown in the legends. (a) Results for very small excitation pulse areas demonstrating the quadratic dependence (black line). (b) Results for a wider range of pulse areas. (c) Results as a function of the excitation pulse length (plotted as a fraction of τ_{HO}). The data were collected with an excitation detuning of $\Delta = 390$ MHz. (d) Ratio of the steady-state and maximum reflectivities as a function of atom-field coupling. The solid line is an exponential fit to the data. (e) Maximum peak reflectivity attained as a function of the atom-field coupling. Here the excitation detuning was varied between $\Delta = 160$ and $\Delta = 390$ MHz to further change the atom-field coupling. The solid line shows the prediction of Eq. (5) with $\alpha = 0.7$ and $\tau_{RN} = 0.18\, \tau_{HO}$.

Raman-Nath limit is violated and the atoms are channeled to the nodes in the potential.

Figure 6(c) shows the same data as Fig. 6(b), plotted as a function of the excitation pulse width, in units of τ_{HO}, for each atom-field coupling strength. Recasting the data in this manner synchronizes the oscillations in reflectivity, revealing the characteristic channeling period predicted by the model in Sec. III (see Fig. 5). This agreement suggests that when the Raman-Nath criterion is violated, the dominant contribution to the signal arises from the macroscopic channeling of the atomic ensemble in the potential. The trends in Fig. 6(c) suggest that our simple model provides an effective method to understand the data. However, a more elaborate model based on density variations in the sample and light propagation through the vapor may be required to understand all features, such as the absence of more than one revival in the reflectivity.

In general, the oscillation period in a sinusoidal potential can be expected to deviate from τ_{HO} in Eq. (3), which is the prediction for a harmonic oscillator potential. These deviations were noted in Ref. [29] and observed over several cycles in Ref. [30] by exposing a BEC to a very shallow optical potential. We note that rescaling the data in the manner presented in Fig. 6(c) allows for a direct observation of the

underlying channeling period for anharmonic potentials of varying depths.

In the same way, this rescaling also reveals the slight dephasing of subsequent oscillations of the reflectivity predicted in Sec. III stemming from experimental sources of decoherence. Figure 6(d) shows the ratio of the steady-state reflectivity to the first maximum in the peak reflectivity as a function of the atom-field coupling strength. We find that this ratio scales inversely as the coupling strength is increased, an aspect that is consistent with the model introduced in Sec. III.

Figure 6(e) shows the maximum peak reflectivity obtained as a function of the atom-field coupling in one-pulse experiments. The solid line shows the predictions of Eq. (5) with an overall scale factor of $\alpha = 0.7$ and $\tau_{RN} = 0.18\,\tau_{HO}$. While the agreement appears reasonable, this comparison demonstrates the sensitivity of the model to τ_{RN}, which we take to be the limit of the Raman-Nath regime. These data also suggest that the highest peak reflectivity is attained for a fairly modest atom-field coupling which optimizes both the momentum-state interference and the channeling effect. Therefore, a larger atom-field coupling is not expected to further enhance the reflectivity. Nevertheless, the first maximum in the peak reflectivity can still be exploited in echo experiments to enhance the grating contrast.

In Fig. 7, we show that the trends in Fig. 6 are replicated in two-pulse (echo) experiments when the width of the first excitation pulse is varied. Comparing the maximum reflectivity [Fig. 7(b)] with the largest reflectivity attained within the Raman-Nath limit [Fig. 7(a)], we find an enhancement of ~ 2 times when the atoms are channeled with a first excitation pulse that violates the Raman-Nath criterion.

Another feature of the echo experiment is that it is possible to further optimize sample reflectivity by varying the duration of the second excitation pulse. Figure 8 shows the reflectivity in an echo experiment in which the second pulse width is varied and the first excitation pulse width is fixed ($\tau_1 = 0.3\,\tau_{HO}$) such that the corresponding one-pulse signal is maximized. Figure 8(a) shows the reflectivity plotted as a function of the second pulse area, while Fig. 8(b) shows the same quantity plotted as a function of the pulse width in units of τ_{HO}. The solid vertical line in Fig. 8(b) shows the Raman-Nath criterion defined by $\tau_2 \approx 0.2\,\tau_{HO}$, and the enhancement in reflectivity achieved by increasing the second pulse length beyond this limit. The reflectivity for various atom-field coupling strengths shows clear maxima which are in phase with respect to the pulse width (as a fraction of τ_{HO}), but not in terms of the pulse area, trends which are similar to those in Figs. 7(b) and 7(c). However, there are no prominent revivals in the reflectivity if the pulse width is further increased.

The enhancement in reflectivity resulting from the use of a second pulse which violates the Raman-Nath criterion has been investigated in Ref. [32] in the presence of a long ($\tau_1 \gg 100\,\tau_{HO}$) lattice pulse that was applied during the trap loading time. Reference [32] reported an overall fourfold enhancement in reflectivity resulting from the use of a non-Raman-Nath pulse after the confinement of atoms at the nodes of the SW lattice potential. As shown in Fig. 8(b), our results suggest that a ~ 2–$3\times$ enhancement is achieved by allowing the second excitation pulse to violate the Raman-Nath
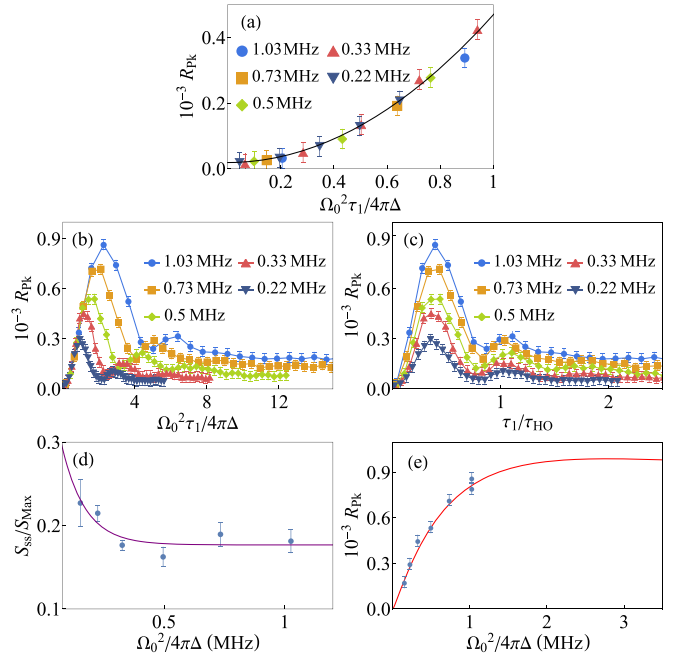

FIG. 7. Peak reflectivity measured in two-pulse grating echo experiments using a variety of atom-field coupling strengths shown in the legends. (a) Results for very small excitation pulse areas with a quadratic fit (black line). (b) Results for a wider range of pulse areas. (c) Results as a function of the excitation pulse length (plotted as a fraction of τ_{HO}). (d) Ratio of steady-state and maximum reflectivities as a function of atom-field coupling. The solid line is an exponential fit to the data. (e) Maximum peak reflectivity attained for each atom-field coupling. The solid line shows the predictions of Eq. (5) with $\alpha = 1$ and $\tau_{RN} = 0.20\,\tau_{HO}$ chosen to match the experimental data. Here, pulse separation $T = 70.2\,\mu s$, second pulse duration $\tau_2 \approx 0.15\,\tau_{HO}$, and excitation detuning $\Delta = 390$ MHz.

criterion, following a first pulse with only $\tau_1 \sim 0.3\,\tau_{HO}$, applied after the confining forces of the MOT are turned off.

When taken together, we find a nearly sixfold enhancement from the combined effects of allowing both excitation pulses to extend beyond the short-pulse limit (see Figs. 7 and 8), as compared to when their lengths are restricted to satisfy the Raman-Nath criterion.
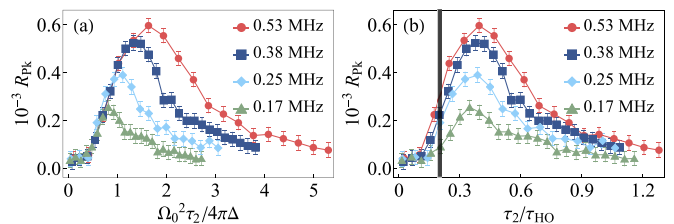

FIG. 8. Peak reflectivity of grating echo experiments as a function of the second pulse duration for various atom-field coupling strengths (shown in the legend). Results are plotted as a function of (a) the pulse area and (b) the pulse duration as a fraction of τ_{HO}. In (b), the vertical line shows the predicted end of the Raman-Nath regime, defined by $\tau_2 \sim 0.2\,\tau_{HO}$. These data were collected using $T = 70.2\,\mu s$, a first excitation pulse of length $\tau_1 = 0.3\,\tau_{HO}$, and an excitation detuning of $\Delta = 160$ MHz.

V. CONCLUSIONS

We have studied channeling oscillations in the reflectivity of atomic gratings in the context of echo experiments. We have demonstrated an improvement in contrast by increasing the length of the excitation pulses beyond the Raman-Nath limit that is complementary to the work in Ref. [32] which relied on lattice loading during the trapping phase. We have explained the results using a simple theoretical model which appears to be applicable to a broad class of experiments in which atoms are channeled using long excitation pulses.

Our results lay the groundwork for achieving further significant improvements in contrast by varying the detuning of the readout pulse and the number of atoms in the cold sample. These effects can be modeled by combining the description of channeling in this paper with a more detailed calculation of the peak reflectivity in samples with variable density [41,42]. Since our apparatus has addressed magnetic field inhomogeneities and improved vibration stability compared to previous experiments [18,19], we expect that the signal enhancement will translate to improved sensitivity of echo experiments on a ∼250 ms timescale.

[1] M. Kasevich and S. Chu, Atomic interferometry using stimulated Raman transitions, Phys. Rev. Lett. **67**, 181 (1991).

[2] A. Peters, K. Y. Chung, and S. Chu, Measurement of gravitational acceleration by dropping atoms, Nature (London) **400**, 849 (1999).

[3] M. J. Snadden, J. M. McGuirk, P. Bouyer, K. G. Haritos, and M. A. Kasevich, Measurement of the Earth's gravity gradient with an atom interferometer-based gravity gradiometer, Phys. Rev. Lett. **81**, 971 (1998).

[4] J. M. McGuirk, G. T. Foster, J. B. Fixler, M. J. Snadden, and M. A. Kasevich, Sensitive absolute-gravity gradiometry using atom interferometry, Phys. Rev. A **65**, 033608 (2002).

[5] Z.-K. Hu, B.-L. Sun, X.-C. Duan, M.-K. Zhou, L.-L. Chen, S. Zhan, Q.-Z. Zhang, and J. Luo, Demonstration of an ultrahigh-sensitivity atom-interferometry absolute gravimeter, Phys. Rev. A **88**, 043610 (2013).

[6] L. Morel, Z. Yao, P. Cladé, and S. Guellati-Khélifa, Determination of the fine-structure constant with an accuracy of 81 parts per trillion, Nature (London) **588**, 61 (2020).

[7] R. H. Parker, C. Yu, W. Zhong, B. Estey, and H. Müller, Measurement of the fine-structure constant as a test of the standard model, Science **360**, 191 (2018).

[8] G. Tino, L. Cacciapuoti, S. Capozziello, G. Lambiase, and F. Sorrentino, Precision gravity tests and the Einstein equivalence principle, Prog. Part. Nucl. Phys. **112**, 103772 (2020).

[9] B. Stray, A. Lamb, A. Kaushik, J. Vovrosh, A. Rodgers, J. Winch, F. Hayati, D. Boddice, A. Stabrawa, A. Niggebaum *et al.*, Quantum sensing for gravity cartography, Nature (London) **602**, 590 (2022).

[10] X. Wu, Z. Pagel, B. S. Malek, T. H. Nguyen, F. Zi, D. S. Scheirer, and H. Müller, Gravity surveys using a mobile atom interferometer, Sci. Adv. **5**, eaax0800 (2019).

[11] A. López-Vázquez, M. Maldonado, E. Gomez, N. Corzo, E. de Carlos-López, J. F. Villafañe, K. Jiménez-García, J. Jimenez-Mier, J. López-González, C. López-Monjaraz *et al.*, Compact laser modulation system for a transportable atomic gravimeter, Opt. Express **31**, 3504 (2023).

[12] B. Battelier, B. Barrett, L. Fouché, L. Chichet, L. Antoni-Micollier, H. Porte, F. Napolitano, J. Lautier, A. Landragin, and P. Bouyer, Development of compact cold-atom sensors for inertial navigation, in *Quantum Optics*, edited by J. Stuhler and A. J. Shields, Proc. SPIE Vol. 9900 (SPIE, Bellingham, WA, 2016), p. 990004.

[13] Y. Bidel, N. Zahzam, C. Blanchard, A. Bonnin, M. Cadoret, A. Bresson, D. Rouxel, and M. Lequentrec-Lalancette, Absolute marine gravimetry with matter-wave interferometry, Nat. Commun. **9**, 627 (2018).

[14] Y. Bidel, N. Zahzam, A. Bresson, C. Blanchard, M. Cadoret, A. V. Olesen, and R. Forsberg, Absolute airborne gravimetry with a cold atom sensor, J. Geodesy **94**, 20 (2020).

[15] C. Freier, M. Hauth, V. Schkolnik, B. Leykauf, M. Schilling, H. Wziontek, H.-G. Scherneck, J. Müller, and A. Peters, Mobile quantum gravity sensor with unprecedented stability, J. Phys.: Conf. Ser. **723**, 012050 (2016).

[16] S. B. Cahn, A. Kumarakrishnan, U. Shim, T. Sleator, P. R. Berman, and B. Dubetsky, Time-domain de Broglie wave interferometry, Phys. Rev. Lett. **79**, 784 (1997).

[17] B. Barrett, I. Chan, C. Mok, A. Carew, I. Yavin, A. Kumarakrishnan, S. B. Cahn, and T. Sleator, Time-domain interferometry with laser-cooled atoms, in *Advances in Atomic, Molecular, and Optical Physics*, edited by E. Arimondo, P. R. Berman, and C. C. Lin, Vol. 60 (Elsevier, Amsterdam, 2011), pp. 119–199.

[18] B. Barrett, A. Carew, S. Beattie, and A. Kumarakrishnan, Measuring the atomic recoil frequency using a modified grating-echo atom interferometer, Phys. Rev. A **87**, 033626 (2013).

[19] C. Mok, B. Barrett, A. Carew, R. Berthiaume, S. Beattie, and A. Kumarakrishnan, Demonstration of improved sensitivity of echo interferometers to gravitational acceleration, Phys. Rev. A **88**, 023614 (2013).

[20] B. Barrett, A. Carew, H. Beica, A. Vorozcovs, A. Pouliot, and A. Kumarakrishnan, Prospects for precise measurements with echo atom interferometry, Atoms **4**, 19 (2016).

[21] I. Abella, N. Kurnit, and S. Hartmann, Photon echoes, Phys. Rev. **141**, 391 (1966).

[22] P. L. Gould, G. A. Ruff, and D. E. Pritchard, Diffraction of atoms by light: The near-resonant Kapitza-Dirac effect, Phys. Rev. Lett. **56**, 827 (1986).

[23] B. Barrett, Techniques for measuring the atomic recoil frequency using a grating-echo atom interferometer, Ph.D. thesis, York University, 2012.

[24] P. J. Martin, P. L. Gould, B. G. Oldaker, A. H. Miklich, and D. E. Pritchard, Diffraction of atoms moving through a standing light wave, Phys. Rev. A **36**, 2495 (1987).

[25] P. J. Martin, P. L. Gould, B. G. Oldaker, A. H. Miklich, and D. E. Pritchard, Diffraction of atoms from a standing light wave, Physica B+C **151**, 255 (1988).

[26] M. Weidemüller, A. Hemmerich, A. Görlitz, T. Esslinger, and T. W. Hänsch, Bragg diffraction in an atomic lattice bound by light, Phys. Rev. Lett. **75**, 4583 (1995).

[27] B. Deh, C. Marzok, S. Slama, C. Zimmermann, and P. W. Courteille, Bragg spectroscopy and Ramsey interferometry with an ultracold Fermi gas, Appl. Phys. B **97**, 387 (2009).

[28] C. S. Adams, M. Sigel, and J. Mlynek, Atom optics, Phys. Rep. **240**, 143 (1994).

[29] S. Dürr, S. Kunze, and G. Rempe, Pendellösung oscillations in second-order Bragg scattering of atoms from a standing light wave, Quantum Semiclassic. Opt.: J. Eur. Opt. Soc. Part B **8**, 531 (1996).

[30] Y. B. Ovchinnikov, J. H. Müller, M. R. Doery, E. J. D. Vredenbregt, K. Helmerson, S. L. Rolston, and W. D. Phillips, Diffraction of a released Bose-Einstein condensate by a pulsed standing light wave, Phys. Rev. Lett. **83**, 284 (1999).

[31] S. Beattie, B. Barrett, M. Weel, I. Chan, C. Mok, S. B. Cahn, and A. Kumarakrishnan, Influence of spontaneous emission on a single-state atom interferometer, Phys. Rev. A **77**, 013610 (2008).

[32] M. F. Andersen and T. Sleator, Lattice interferometer for laser-cooled atoms, Phys. Rev. Lett. **103**, 070402 (2009).

[33] G. Carlse, A. Pouliot, T. Vacheresse, A. Carew, H. Beica, S. Winter, and A. Kumarakrishnan, Technique for magnetic moment reconstruction of laser-cooled atoms using direct imaging and prospects for measuring magnetic sublevel distributions, J. Opt. Soc. Am. B **37**, 1419 (2020).

[34] H. C. Beica, A. Pouliot, A. Carew, A. Vorozcovs, N. Afkhami-Jeddi, G. Carlse, P. Dowling, B. Barron, and A. Kumarakrishnan, Characterization and applications of auto-locked vacuum-sealed diode lasers for precision metrology, Rev. Sci. Instrum. **90**, 085113 (2019).

[35] A. Pouliot, H. C. Beica, A. Carew, A. Vorozcovs, G. Carlse, B. Barrett, and A. Kumarakrishnan, Investigations of optical pumping for magnetometry using an auto-locking laser system, in *Laser Technology for Defense and Security XIV*, edited by M. Dubinskiy and T. C. Newell, Proc. SPIE Vol. 10637 (SPIE, Bellingham, WA, 2018), p. 106370A.

[36] A. Vorozcovs, M. Weel, S. Beattie, S. Cauchi, and A. Kumarakrishnan, Measurements of temperature scaling laws in an optically dense magneto-optical trap, J. Opt. Soc. Am. B **22**, 943 (2005).

[37] M. Sargent III, M. O. Scully, and W. E. J. Lamb, *Laser Physics* (Addison-Wesley Publishing Company, Reading, MA, 1974).

[38] P. P. Ewald, Zur Begründung der Kristalloptik, Annal. Phys. **354**, 1 (1916).

[39] N. Kato and A. R. Lang, A study of Pendellösung fringes in X-ray diffraction, Acta Crystallogr. **12**, 787 (1959).

[40] Note that Eqs. (1) and (2) include a contribution from spontaneous emission in the form of the parameter θ. However, this leads only to a phase shift of the scattered field signal as described in Ref. [31].

[41] A. Schilke, C. Zimmermann, P. W. Courteille, and W. Guerin, Photonic band gaps in one-dimensionally ordered cold atomic vapors, Phys. Rev. Lett. **106**, 223903 (2011).

[42] S. Slama, C. von Cube, M. Kohler, C. Zimmermann, and P. W. Courteille, Multiple reflections and diffuse scattering in Bragg scattering at optical lattices, Phys. Rev. A **73**, 023424 (2006).